Second yield via dislocation-induced premelting in copper

L. Wang,[1,2] Y. Cai,[1,3] A. M. He,[4] and S. N. Luo[1,2,*]

[1]*The Peac Institute of Multiscale Sciences, Chengdu, Sichuan 610031, People's Republic of China*

[2]*Key Laboratory of Advanced Technologies of Materials, Ministry of Education, Southwest Jiaotong University, Chengdu, Sichuan, 610031, People's Republic of China*

[3]*CAS Key Laboratory of Materials Behavior and Design, Department of Modern Mechanics, University of Science and Technology of China, Hefei, Anhui 230027, People's Republic of China*

[4]*Institute of Applied Physics and Computational Mathematics, Beijing 100094, People's Republic of China*

(Received 5 January 2016; revised manuscript received 23 March 2016; published 10 May 2016)

Premelting or virtual melting was proposed previously as an important deformation mechanism for high strain-rate loading. However, two questions remain outstanding: how premelting occurs exactly, and whether it plays a role in plastic deformation independent of, parasitic on, or synergetic with, dislocation motion. By virtue of double-shock compression, our large-scale molecular dynamics simulations reveal two yields in single-crystal copper, with the first yield achieved via dislocation motion, and the second, via dislocation-induced premelting as well. The clean capture of melting during dislocation motion suggests that premelting occurs on slip planes and at their intersections, facilitating gliding and leading to yield together with dislocation motion.

DOI: 10.1103/PhysRevB.93.174106

I. INTRODUCTION

Premelting, i.e., localized melting at temperatures below the equilibrium melting point (T_m), has been a subject of interest and mystery for more than a century [1,2]. Most experiments [3–5] and theories [6–10] attribute premelting to point defects (vacancies and interstitials) [11–14], and planar defects, such as surfaces [15–17] and grain boundaries [18–20], which lower the energy barrier to liquid nucleation and effectively prevent superheating of a solid [21]. Premelting at dislocations, another type of defect which represents the predominant mechanism of plastic deformation [22], was also proposed [23]. Direct observation of premelting at dislocations within a crystal is extremely difficult given the small size and complex morphologies involved. With real-time video microscopy, premelting was observed in colloidal crystals at pseudodislocations [24] with sizes far beyond real dislocations (μm versus nm).

In molecular dynamics (MD) simulations, negligible premelting at a partial dislocation (stacking fault) was observed for copper [25], while substantial premelting in copper single crystals was reported for shock loading along ⟨110⟩ and ⟨111⟩, and attributed to solid-state disordering prior to melting [26]. Premelting appears to be a common, short-lived phenomenon in single crystals under shock loading [26–31]. Although it represents a supercooling state and is highly transient in nature, premelting arguably plays a key role in phase transitions and plastic deformation. For instance, crystal-amorphous and crystal-crystal transformations can be achieved via premelting or virtual melting by removing athermal friction, increasing atomic mobility, and decreasing kinetic barriers [32–36]. Premelting or virtual melting can serve as a plastic deformation mechanism for high strain-rate loading including shock compression; it is argued that high deviatoric stress leads to premelting [29,30] and boosted plastic flow beyond traditional mechanisms of plasticity. While its existence and involvement with plastic deformation are definitive, some key questions remain open: how premelting occurs exactly, and whether it plays a role in plastic deformation independent of, parasitic on, or synergetic with, dislocation motion.

In order to address these outstanding questions of fundamental and applied merits for dynamic extreme conditions, we implement a double-shock, as opposed to conventional single-shock, scheme in large-scale MD simulations of single-crystal copper under shock compression. Experimentally, double-shock loading or reverberation shocks have long been exploited to investigate high-pressure yield strength and phase changes, and to mimic quasi-isentropic compression [37,38]. The ultrafast dynamics of dislocation motion and premelting in single-shock loading renders it difficult to distinguish melting from dislocations [26,30], while double or reverberating shocks slow down the dynamics, thus advantageous for analysis. Double-shock compression leads to two yields: the first yield is achieved via dislocation motion, and the second, via dislocation-induced premelting. The clean capture of melting during dislocation motion suggests that premelting occurs on slip planes and at their intersections, facilitating gliding and leading to yield together with dislocation motion. Our results reveal the exact nature of premelting and its interplay with dislocation motion, establishing premelting as an important mechanism for plastic deformation, and likely, phase transitions.

II. METHODOLOGY

For MD simulations of double-shock loading, the Large-scale Atomic/Molecular Massively Parallel Simulator [39] and an embedded atom potential of Cu [40] are utilized. The accuracy of this interatomic potential has been verified by numerous shock and nonshock simulations, especially in describing thermodynamic and mechanical properties [41–43], high pressure melting [28,44], and equation of state [45]. The system size is approximately 7.5 million atoms, and the dimensions are $\sim 820 \times 10 \times 10$ nm^3 along the x-[110], y-[001], and $z - [1\bar{1}0]$ directions, respectively.

*sluo@pims.ac.cn; sluo@swjtu.cn

A larger system is also attempted to examine possible size effects, which comprises 24 million atoms with doubled cross sections ($\sim 720 \times 20 \times 20$ nm^3). The shock direction is along the x axis or [110]. Prior to shock loading, the configurations are relaxed at 0 K, and then thermalized with the constant-pressure-temperature ensemble under three-dimensional periodic conditions at 300 K and zero pressure.

Shock simulations are performed with the microcanonical ensemble. The shock direction (the x direction) is chosen to be [110] for its well manifested elastic-plastic transition. Periodic boundary conditions are applied only along the transverse directions (the y and z directions). The time step for integration of the equation of motion is 1 fs. The small region on the left is set as the piston [46,47] in our shock simulations. The interactions between the piston and the rest of the atoms in the configuration are described with the same interatomic potential, while the atoms in the piston do not participate in molecular dynamics. In order to avoid overwhelmingly abundant homogeneous nucleation of dislocations incurred by single shocks, and thus simplify analysis, we apply double-shock loading instead. An atomic piston [47] delivers the first shock with a piston velocity of $u_\mathrm{p} = 0.75$ km s^{-1} at time $t = 0$; the first shock is intended to induce an elastic-plastic transition (the first yield), emitting dislocations without melting. For the second shock, we examine piston velocities up to 3 km s^{-1}. The second shock is initiated at $t = 100$ ps, leading to a second yield either with solid-state disordering (e.g., $u_\mathrm{p} = 1.5$ km s^{-1}), and/or apparent premelting (e.g., $u_\mathrm{p} = 2.5$ km s^{-1}) along the pre-existing dislocations induced by the first shock.

To quantify structural disordering of a specimen during shock loading, local order parameter Q_6 is utilized, which measures the symmetry correlation of an atom with its nearest neighbors [48,49]. We perform 1D binning analyses [44,50] to resolve spatially physical properties including stress σ_{ij} $(i,j = x,y,z)$, Q_6, and temperature (T) profiles along the wave propagation direction. The binning width is 0.5 nm. To calculate T and σ_{ij} within each bin, we either remove its center-of-mass velocity $\bar{v}_i$ $(i = x,y,$ and $z)$, or apply corrections $\Delta T = -(m/3k_\mathrm{B})(\bar{v}_x^2 + \bar{v}_y^2 + \bar{v}_z^2)$ and $\Delta\sigma_{ij} = -(m/V_a)\bar{v}_i\bar{v}_j$, where m is the atomic mass, V_a is the atomic volume averaged over the bin, and k_B is Boltzmann's constant. The pressure is obtained as $P = (\sigma_{xx} + \sigma_{yy} + \sigma_{zz})/3$. We here define $2\tau = \sigma_{xx} - \frac{1}{2}(\sigma_{yy} + \sigma_{zz})$, where τ denotes shear stress. The common neighbor analysis [51,52] and dislocation network analysis [53,54] are also implemented to characterize local structure around an atom. In our simulations, we also analyze dynamic deformation with pole figures [55], obtained following standard electron backscatter diffraction or EBSD analysis [56,57].

III. RESULTS AND DISCUSSION

Our simulations show similar results for two configurations with different cross sections, that is, the system size effect can be neglected for the purpose of this work. We use the smaller system ($820 \times 10 \times 10$ nm^3) for the following discussion. Figure 1(a) shows complete wave features during double-shock loading with $u_\mathrm{p} = 0.75$ and 2.5 km s^{-1}: the first shock induces an elastic-plastic transition (E-P1) with a peak stress of $\sim$37 GPa; upon reshock (P1-P2), the solid undergoes a second yield and reaches a peak stress of $\sim$169 GPa. Since our main interest lies in the P1-P2 transition region as indicated by the rectangle [the dash-dotted lines in Fig. 1(a)], blown up in Fig. 1(b), we detail in Figs. 1(c)–1(f) the corresponding dislocation structure, atomic configuration, and profiles of pressure (P), shear stress (2τ), temperature (T), and local order parameter (Q_6) along the shock direction. Pressure and temperature increase as the second plastic shock evolves into a stable shock. For convenience, we divide the P1-P2 transition zone into four subregions, A–D, according to different features in the wave profiles of u_p, 2τ, and Q_6 and in the microstructures. The boundaries between them are depicted with dash lines in Figs. 1(b)–1(f).

For P1 (region A), there are four slip systems, namely $(111)[11\bar{2}]$, $(11\bar{1})[112]$, $(1\bar{1}1)[\bar{1}12]$, and $(1\bar{1}\bar{1})[1\bar{1}2]$, activated, which form a highly regular dislocation pattern following their slip planes [Fig. 1(c)]. Upon reshock (B), 2τ increases to a peak succeeded by its relaxation [Fig. 1(e)], indicating a second yield which completes in region C. This yield leads to shorter, "chaotic" dislocation loops along with dissolving of dislocation structure at the intersections of slip planes and partially on slip planes, in contrast to the regular dislocation pattern in regions A and B. However, the regular pattern is partially restored in region D, but with denser, smaller, random dislocations. The pattern changes in dislocations coincide with those in Q_6 [Fig. 1(d)]; the disruption and partial restoration of dislocation pattern, as well as the appearance of new dislocations, concur with atomic-level or bin-averaged decrease or increase in Q_6 [Figs. 1(d) and 1(f)]. In other words, local disordering leads to annihilation of dislocations, since the latter still requires a high degree of structure order in terms of face-centered cubic (fcc) and hexagonal close-packed packings (hcp). The local disordering could be amorphization (solid-state disordering) or premelting, since temperature lies well below the equilibrium melting temperature $T_\mathrm{m}(P)$ [26], less than $0.6T_\mathrm{m}$ [Fig. 1(f)]. On the other hand, a natural explanation for subsequent partial order recovering in region C is recrystallization of disordered solid or liquid.

To further characterize local structure changes during plastic deformation in terms of crystal orientation, we perform pole figure analysis [55] of the atomic configurations at different stages, similar to those based on electron back-scattering or x-ray diffraction. As shown in Fig. 2, the pole figure remains almost identical in regions A and B, while the most pronounced change occurs in region C during the second yield: the four spots in the $\{110\}$ pole figure reduce to three spots, along with pronounced rotation (10°) of two major spots, and the appearance of minor spots, indicating grain rotation and grain refinement. In region D, the spots disappeared in C appear again in D with reduced intensities, indicating recrystallization.

In sharp contrast, for the second shock with $u_\mathrm{p} = 1.5$ km s^{-1}, dislocations proceed to propagate along their slip planes, and local disordering is much less pronounced compared to $u_\mathrm{p} = 2.5$ km s^{-1}. The regular dislocation pattern remains behind the second shock front during shear stress relaxation upon reshock. Consistently, the pole figures show no apparent change during the whole process.

However, it is inadequate to claim premelting at $u_\mathrm{p} = 2.5$ km s^{-1} simply from local structures and shear stress

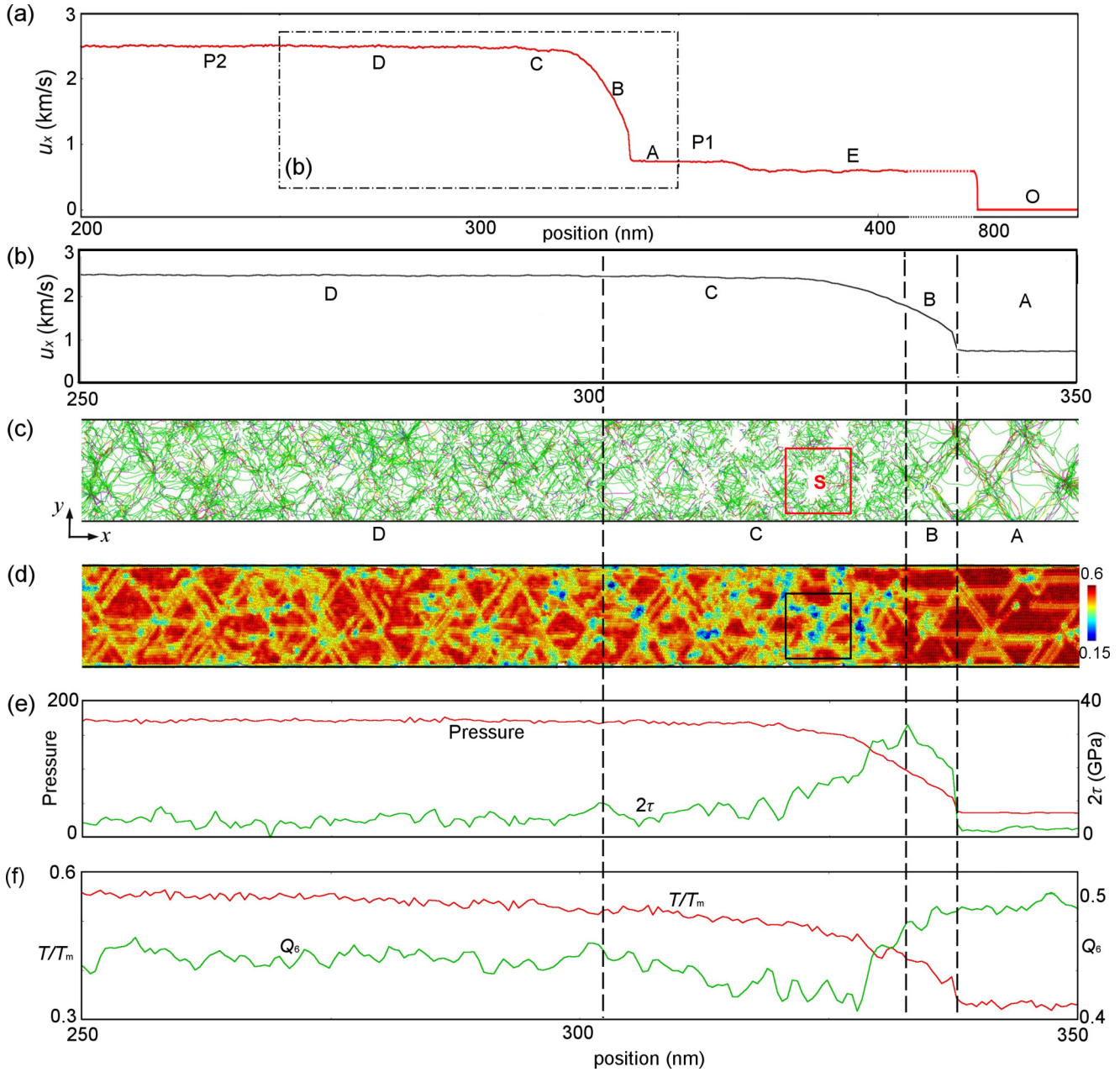

FIG. 1. (a) Particle velocity profile $u_x(x)$ for double-shock loading, at $u_p = 0.75$ and 2.5 km s^{-1}. O: unshocked; E: elastic wave; P1: the first plastic shock after the first yield; P2: the second plastic shock after the second yield. (b) Particle velocity profile $u_x(x)$ corresponding to the range indicated by the rectangle in (a). (c) Dislocation structure of the region undergoing the second yield. (d) Atomic configuration, with color coding based on local order parameter Q_6. Red refers to solid, and blue, liquid or amorphous structure. (e) Pressure and shear stress (2τ) profiles along the shock direction. (f) Temperature and Q_6 profiles; the boundary between C and D is determined with Q_6. Temperature is normalized by the equilibrium melt temperature T_m at the corresponding shock pressure. (b)–(f) The spatial range delimited within the rectangle in (a). A: P1; B–D: reshock region; B: the second yield; C: dislocation-induced premelting; D: complete recrystallization. t: 130 ps. Shock direction: left → right, along [110].

profiles, since amorphous solids and supercooled liquids have similar structure characteristics for copper [58]. The most definitive indicator distinguishing a melt from crystalline and amorphous solids is self-diffusion coefficient D, which can be calculated with the Einstein expression [59]

$$D = \lim_{t\to\infty} \frac{1}{6t} \mathrm{MSD}(t), \tag{1}$$

from mean square displacement MSD,

$$\mathrm{MSD}(t) = \langle |r(t) - r(0)|^2 \rangle. \tag{2}$$

Here t denotes time, r is the atomic position, and $\langle \cdots \rangle$ denotes averaging over ensemble only. In order to achieve longer equilibration durations for calculating MSD, Lennard-Jones absorbing walls [31,60] are applied to a selected region with the wall velocity equaling to average particle velocity in

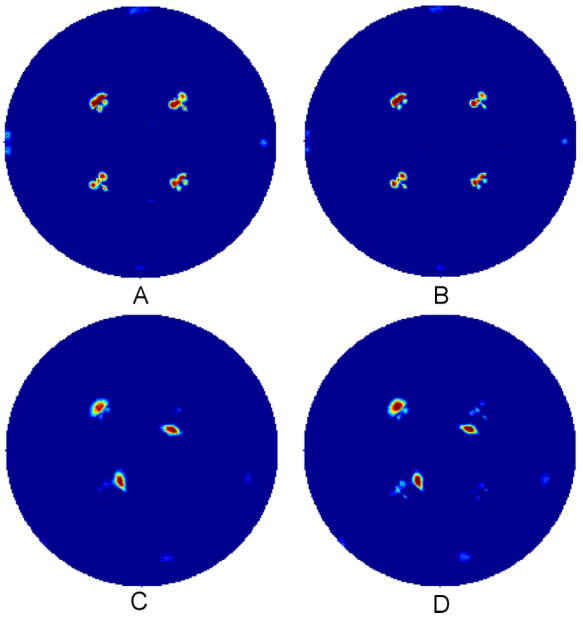

FIG. 2. {110} pole figures of the regions at different shock stages. Regions A–D are defined in Fig. 1.

the region under consideration. No additional constrains are applied to the classical trajectories beyond shock loading and absorbing walls.

The evolution of MSDs in different regions (regions A, C, and D) during the extended equilibration period are shown in Fig. 3. MSD(t) for region C exhibits two distinct stages: rapid increase during the first 0–8 ps ($D \sim 10^{-6}$ cm^2 s^{-1}), which is attributed to dislocation-induced premelting, and followed by slower increase ($D \sim 10^{-8}$ cm^2 s^{-1}), owing to recrystallization of supercooled melts. In contrast, MSDs in regions A and D remain approximately constant, with $D \sim 10^{-8}$ cm^2 s^{-1}. The difference of two orders of magnitude in D between region C and regions A and D implies a partial melting in region C, and solid state in regions A (no premelting) and D (recrystallization). The differences in diffusion coefficient are also consistent with the inverse pole figures in Fig. 2.

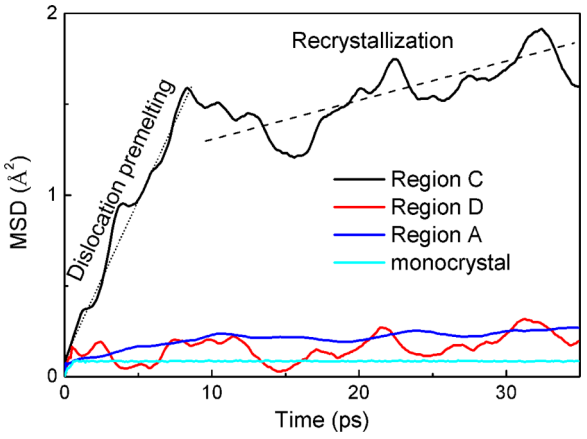

FIG. 3. Time evolution of MSDs in regions A (P1), C, D (P2), and in monocrystal Cu without dislocations at $T = 2800$ K and $P = 169$ GPa. The dotted and dashed lines indicate dislocation-induced premelting and recrystallization in region C, respectively.

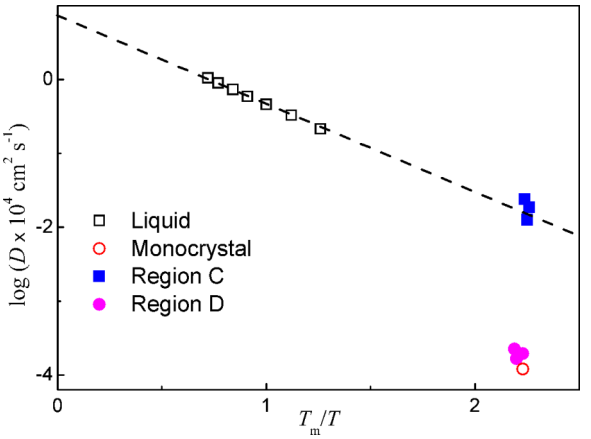

FIG. 4. Diffusion coefficients as a function of temperature, of liquid Cu (empty squares), and monocrystal Cu without any defects (empty circles) at 169 GPa, and in the premelted regions (filled squares; different locations in region C), and after recrystallization following premelting (filled circles; different locations in region D). The dashed line is the Arrhenius plot for liquid Cu. Also see Fig. 1.

To further verify that partial melting occurs in region C, we compare diffusion coefficients in region C with those of liquid and solid copper at the same pressure (∼169 GPa, Fig. 4). D values in three different locations in region C (as well as in region D) are computed for statistical purpose. Temperature is varied for liquid copper in order to obtain an Arrhenius plot, and its extension to $T_m/T > 1$ represents supercooled liquid. D values in region C during "partial premelting" after the second yield lie on the liquid Arrhenius plot in the supercooling regime, and are higher than those in region D (recrystallization) by two orders of magnitude. In addition, we compute MSD of a Cu single crystal without dislocations at similar temperature (2800 K) and pressure (169 GPa), and the corresponding diffusion coefficient $D \sim 10^{-8}$ cm^2 s^{-1} is similar to those in regions A and D, but about two orders of magnitude lower than that in region C (Figs. 3 and 4). Therefore, transient premelting indeed occurs in region C and contributes partially to disordering, while dislocation self-interactions should not be held responsible for the elevated diffusion in region C. We also examine different piston velocities for the second shock $u_p = 2.0$, 2.25, 2.75, and 3 km s^{-1}, and observe partial premelting at dislocations; $D \sim 10^{-6}$–10^{-5} cm^2 s^{-1} in the melted locations within region C.

During the first yield ($u_p = 0.75$ km s^{-1}), there are negligible disordering and orientation changes (as seen from pole figures), and the diffusion coefficient is similar to those of solids. Thus, the first yield is achieved via dislocation motion only, while the second ($u_p = 2.5$ km s^{-1}) via premelting in addition to dislocation motion. This premelting is highly transient as a result of a large degree of supercooling [61], and drastically different from thermodynamic (equilibrium) melting. Premelting is actually parasitic on dislocation motion, and they collectively give rise to plastic flow. We choose an area centered around region S in Fig. 1(c) to illustrate the details of premelting, and its relation to dislocation motion. The snapshots in Fig. 5 capture the sequence of dislocation motion, premelting, and subsequent recrystallization,

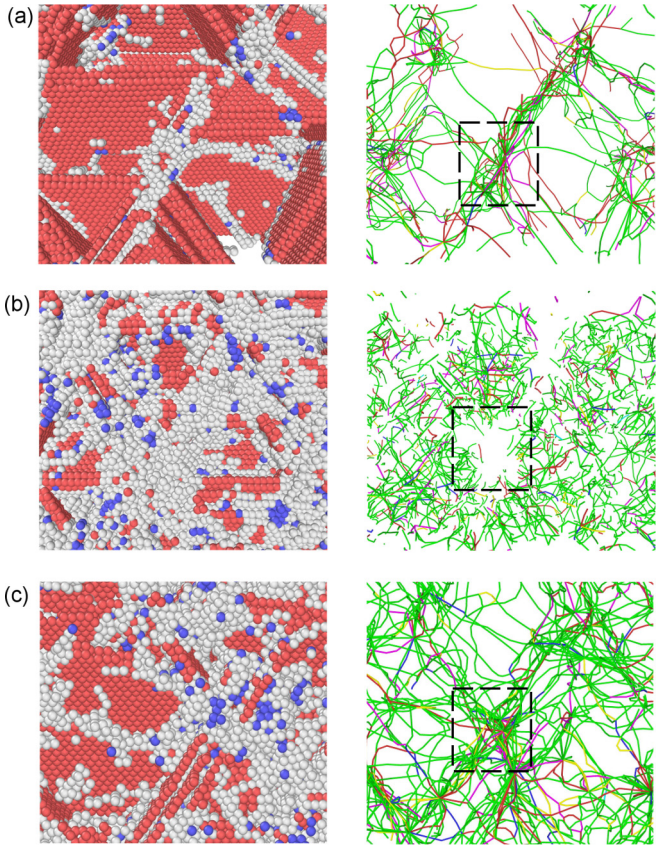

FIG. 5. Snapshots of atomic configurations (left column) and corresponding dislocation structures (right column): (a) 125 ps, (b) 130 ps, and (c) 135 ps. Only atoms in hcp (red), body-centered cubic (blue), and disordered (gray) local structures are displayed. The dashed square corresponds to of the square labeled as S in Figs. 1(c) and 1(d).

visualized with common neighbor analysis (the left column) and dislocation network analysis (the right column).

Dislocations/stacking faults nucleate and propagate until they intersect each other during the passage of the first shock (125 ps, the first yield). Local disordering rather than melting ensues as a result of the activation of slip systems and their interactions [Fig. 5(a)]. Upon compression by the second shock (130 ps) which leads to the second yield, melting originates from the disordered regions (the intersections of slip planes), and then spreads along the slip planes [Fig. 5(b)]. This melting occurs at temperatures well below the thermodynamic melting temperature [Fig. 1(f)], and thus premelting. Premelting is very localized, and the majority of the volume under consideration is still solid. The corresponding dislocation lines change from long and "ordered" [Fig. 5(a)] to short and chaotic [Fig. 5(b)], with some old ones annihilated and new, shorter ones nucleated. The dislocation lines annihilated are mostly located on the slip planes previously activated [Fig. 5(a)], coinciding with the regions under premelting. Since shear deformation relaxes shear stress at this stage, premelting actually complements dislocation motion in plastic flow. Premelting is highly unstable, so it lasts only for a few picoseconds and heterogeneous crystallization takes over [135 ps, Fig. 5(c)]. During crystallization, crystalline order is restored in previously melted regions, and defects in the form of dislocations also "restore". On the other hand, dislocations are partially "annealed" at locations away from the main slip planes. Therefore, premelting is indeed induced by dislocation motion and synergetic with dislocation motion in plastic deformation.

The local temperature at dislocations for a shock pressure of ∼169 GPa is determined to be ∼2850 K, and only slightly higher than those in "undeformed" regions (∼2730 K), both well below the thermodynamic melting temperature under this shock pressure ($T_m \approx 4920$ K). Therefore, dislocation-induced premelting is attributed to the lowered energy barrier to melting by solid-state disordering (similar to premelting at planar defects [2]) during the interaction of dislocations and dislocation motion, rather than dislocation-induced "hotspots" [62]. Since trivial disordering is involved in heating of a partial dislocation without dislocation motion, premelting is negligible as well [25]. Although we deliberately design a double-shock scheme to better resolve premelting during dislocation motion, the mechanism of premelting and its role in plastic deformation still apply to premelting under single shocks [26–30]. During single shock loading, homogeneous activation of slip systems and their growth are explosive, leading to higher temperature (compared to double-shock compression), faster dislocation nucleation, motion and interactions, and consequently, accelerated transition from dislocation motion to localized premelting, which is too rapid to resolve even at MD scales.

IV. CONCLUSION

Our MD simulations demonstrate that premelting within single-crystal Cu during shock compression is induced by dislocation motion and dislocation interactions. The double-shock method allows for a clean capture of premelting on slip planes during dislocation motion. Solid-state disordering from dislocation interactions, rather than dislocation-induced hotspots, is the predominant cause of premelting. While it is highly transient and terminated by recrystallization, premelting facilitates gliding along parent slip planes, synergetic with dislocation motion in assisting plastic flow.

ACKNOWLEDGMENT

This work was partially supported by the 973 Project of China (No. 2014CB845904) and National Natural Science Foundation of China (No. 11402032).

[1] F. A. Lindemann, Phys. Z **11**, 609 (1910).
[2] J. G. Dash, A. W. Rempel, and J. S. Wettlaufer, Rev. Mod. Phys. **78**, 695 (2006).
[3] J. W. M. Frenken and J. F. van der Veen, Phys. Rev. Lett. **54**, 134 (1985).
[4] U. Dahmen, H. Hagege, F. Faudot, T. Radetic, and E. Johnson, Philos. Mag. **84**, 2651 (2004).
[5] M. E. Glicksman and C. L. Vold, Surf. Sci. **31**, 50 (1972).
[6] J. Berry, K. R. Elder, and M. Grant, Phys. Rev. B **77**, 224114 (2008).

[7] Y. Mishin, W. J. Boettinger, J. A. Warren, and G. B. McFadden, Acta Mater. **57**, 3771 (2009).

[8] A. Adland, A. Karma, R. Spatschek, D. Buta, and M. Asta, Phys. Rev. B **87**, 024110 (2013).

[9] E. S. Thomson, L. Benatov, and J. S. Wettlaufer, Phys. Rev. E **82**, 039907(E) (2010).

[10] Y. H. Li, L. Wang, B. Li, J. C. E, F. P. Zhao, J. Zhu, and S. N. Luo, J. Chem. Phys. **142**, 054706 (2015).

[11] A. V. Granato, Phys. Rev. Lett. **68**, 974 (1992).

[12] S. C. Glotzer, J. Non-Cryst. Solids **274**, 342 (2000).

[13] K. Nordlund, Y. Ashkenazy, R. S. Averback, and A. V. Granato, Europhys. Lett. **71**, 625 (2005).

[14] M. Forsblom and G. Grimvall, Phys. Rev. B **72**, 054107 (2005).

[15] R. Lipowsky, U. Breuer, K. C. Prince, and H. P. Bonzel, Phys. Rev. Lett. **62**, 913 (1989).

[16] R. W. Cahn, Nature (London) **323**, 668 (1986).

[17] W. A. Curtin, Phys. Rev. B **39**, 6775 (1989).

[18] R. W. Cahn, Nature (London) **413**, 582 (2001).

[19] G. Ciccotti, M. Guillope, and V. Pontikis, Phys. Rev. B **27**, 5576 (1983).

[20] R. Lipowsky, Phys. Rev. Lett. **57**, 2876 (1986).

[21] B. Pluis, A. W. Denier van der Gon, J. W. M. Frenken, and J. F. van der Veen, Phys. Rev. Lett. **59**, 2678 (1987).

[22] H. J. Frost and M. F. Ashby, *Deformation-Mechanism Maps: The Plasticity and Creep of Metals and Ceramics* (Pergamon press, New York, 1982).

[23] L. Burakovsky, D. L. Preston, and R. R. Silbar, Phys. Rev. B **61**, 15011 (2000).

[24] A. M. Alsayed, M. F. Islam, J. Zhang, P. J. Collings, and A. G. Yodh, Science **309**, 1207 (2005).

[25] L. B. Han, Q. An, R. S. Fu, L. Q. Zheng, and S. N. Luo, J. Chem. Phys. **130**, 024508 (2009).

[26] Q. An, S. N. Luo, L. B. Han, L. Q. Zheng, and O. Tschauner, J. Phys. Condens. Matter **20**, 095220 (2008).

[27] C. J. Wu, P. Soderlind, J. N. Glosli, and J. E. Klepeis, Nat. Mater. **8**, 223 (2009).

[28] A. M. He, P. Wang, J. L. Shao, S. Q. Duan, F. P. Zhao, and S. N. Luo, J. Appl. Phys. **115**, 143503 (2014).

[29] R. Ravelo, T. C. Germann, O. Guerrero, Q. An, and B. L. Holian, Phys. Rev. B **88**, 134101 (2013).

[30] V. Levitas and R. Ravelo, Proc. Natl. Acad. Sci. USA **109**, 13204 (2012).

[31] M. M. Budzevich, V. V. Zhakhovsky, C. T. White, and I. I. Oleynik, Phys. Rev. Lett. **109**, 125505 (2012).

[32] V. I. Levitas, B. F. Henson, L. B. Smilowitz, and B. W. Asay, Phys. Rev. Lett. **92**, 235702 (2004).

[33] V. I. Levitas, Phys. Rev. Lett. **95**, 075701 (2005).

[34] V. I. Levitas, B. F. Henson, L. B. Smilowitz, and B. W. Asay, J. Phys. Chem. B **110**, 10105 (2006).

[35] V. I. Levitas, Z. H. Ren, Y. W. Zeng, Z. Zhang, and G. R. Han, Phys. Rev. B **85**, 220104 (2012).

[36] Y. Peng, F. Wang, Z. R. Wang, A. M. Alsayed, Z. X. Zhang, A. G. Yodh, and Y. L. Han, Nat. Mater. **14**, 101 (2015).

[37] H. Huang and J. R. Asay, J. Appl. Phys. **101**, 063550 (2007).

[38] J. M. Winey, J. N. Johnson, and Y. M. Gupta, J. Appl. Phys. **112**, 093509 (2012).

[39] S. Plimpton, J. Comput. Phys. **117**, 1 (1995), also see http://lammps.sandia.gov.

[40] Y. Mishin, M. J. Mehl, D. A. Papaconstantopoulos, A. F. Voter, and J. D. Kress, Phys. Rev. B **63**, 224106 (2001).

[41] L. Q. Zheng, Q. An, Y. Xie, Z. H. Sun, and S. N. Luo, J. Chem. Phys. **127**, 164503 (2007).

[42] E. M. Bringa, J. U. Cazamias, P. Erhart, J. Stolken, N. Tanushev, B. D. Wirth, R. E. Rudd, and M. J. Caturla, J. Appl. Phys. **96**, 3793 (2004).

[43] S. N. Luo, L.-B. Han, Y. Xie, Q. An, L. Q. Zheng, and K. Xia, J. Appl. Phys. **103**, 093530 (2008).

[44] Y. Cai, L. Wang, H. A. Wu, M. H. Zhu, C. L. Liu, and S. N. Luo, Phys. Rev. B **92**, 014108 (2015).

[45] A. M. He, S. Q. Duan, J. L. Shao, P. Wang, and S. N. Luo, J. Chem. Phys. **139**, 074502 (2013).

[46] B. L. Holian, Shock Waves **5**, 149 (1995).

[47] B. L. Holian and P. S. Lomdahl, Science **280**, 2085 (1998).

[48] P. J. Steinhardt, D. R. Nelson, and M. Ronchetti, Phys. Rev. B **28**, 784 (1983).

[49] P. R. ten Wolde, M. J. Ruiz-Montero, and D. Frenkel, Phys. Rev. Lett. **75**, 2714 (1995).

[50] S. N. Luo, Q. An, T. C. Germann, and L. B. Han, J. Appl. Phys. **106**, 013502 (2009).

[51] D. Faken and H. Jonsson, Comput. Mater. Sci. **2**, 279 (1994).

[52] H. Tsuzuki, P. S. Branicia, and J. P. Rino, Comput. Phys. Commun. **177**, 518 (2007).

[53] A. Stukowski, Modell. Simul. Mater. Sci. Eng. **18**, 015012 (2010).

[54] V. V. Bulatov, L. L. Hsiung, M. J. Tang, A. Arsenlis, M. C. Bartelt, W. Cai, J. N. Florando, M. Hiratani, M. Rhee, G. Hommes, T. G. Pierce, and T. D. de la Rubia, Nature (London) **440**, 1174 (2006).

[55] L. Wang, J. C. E, Y. Cai, F. Zhao, D. Fan, and S. N. Luo, J. Appl. Phys. **117**, 084301 (2015).

[56] H. J. Bunge, *Quantitative Texture Analysis* (DGM-Informationsgesellschaft, Oberursel, 1981).

[57] V. Randle and O. Engler, *Introduction of Texture Analysis Macrotexture, Microtexture and Orientation Mapping* (CRC, Boca Raton, FL, 2000).

[58] Q. An, S. N. Luo, W. A. Goddard III, W. Z. Han, B. Arman, and W. L. Johnson, Appl. Phys. Lett. **100**, 041909 (2012).

[59] D. C. Rapaport, *The Art of Molecular Dynamics Simulation* (Cambridge University Press, Cambridge, 1995).

[60] F. P. Zhao, Q. An, B. Li, H. A. Wu, W. A. Goddard, III, and S. N. Luo, J. Appl. Phys. **113**, 063516 (2013).

[61] S. N. Luo, T. J. Ahrens, T. Cagin, A. Strachan, W. A. Goddard, III, and D. C. Swift, Phys. Rev. B **68**, 134206 (2003).

[62] Y. Cai, F. P. Zhao, Q.An, H. A. Wu, W. A. Goddard, III, and S. N. Luo, J. Chem. Phys. **139**, 164704 (2013).